

Characterizing X-ray Variability of TeV Blazars

Jun Kataoka*

Tokyo Institute of Technology, 2-12-1, Ohokayama, Meguro, Tokyo, Japan

E-mail: kataoka@phys.titech.ac.jp

In this review, I will discuss how to characterize synchrotron X-ray variability of TeV blazars by using the observed/simulated light curves. Apparently, temporal studies provide independent and complementary information to the spectral studies, but surprisingly little attention has been paid especially for the blazar study. Only exception is a classical argument for presence of “time lag”, which may (or may not) reflect the difference of synchrotron cooling timescale. Also very recently, it was suggested that the X-ray variability of TeV blazars indicates a strong red-noise, compared to a fractal, flickering-noise of Seyfert galaxies. Various temporal techniques are proposed in literature, e.g., the power spectrum density (PSD), the structure function (SF), and the discrete correlation function (DCF) and other analysis tools, but special care must be taken if the data are not well sampled and observation is relatively short compared to a characteristic timescale of the system. Also, the situation is being more complicated for low-Earth orbit satellites, e.g., *ASCA*, *RXTE* and *BeppoSAX*, since the light curve inevitably contains “periodic gap” due to the Earth occultation (every $\simeq 6$ sec). I will present detailed approaches to see how the “gap” and the “finite length” of the data affects the results of temporal analysis, and to what extent we can believe in our results. Finally, I will briefly comment on the high-sensitivity X-ray observations with *MAXI*, that may shed new light on the forthcoming *GLAST* era.

Workshop on Blazar Variability across the Electromagnetic Spectrum

April 22-25 2008

Palaiseau, France

*Speaker.

1. Introduction

Blazars are commonly variable from radio to γ -rays. The variability timescale is shortened and the radiation is strongly enhanced by relativistic beaming. For extragalactic TeV sources, the X-ray/TeV γ -ray bands correspond to the highest energy ends of the synchrotron/inverse-Compton emission, which are produced by electrons accelerated up to the maximum energy (e.g., Inoue & Takahara 1996; Krik, Rieger & Mastichiadis 1998). At the highest energy ends, variability is expected to be most pronounced, and in fact, such large flux variations are observed, on a timescale of hours to days (e.g., Kataoka et al. 2001; Tanihata et al. 2001) or even shorter (minutes scale; Aharonian et al. 2007; Albert et al. 2007). Thus the X-ray/TeV variability can be the most direct way to probe the dynamics operating in jet plasma, in particular compact regions of shock acceleration which are presumably close to the central engine.

‘Snapshot’ multiwavelength spectra principally provide us with clues on the emission mechanisms and physical parameters inside relativistic jets. On the other hand, detailed studies of time variability not only lead to complementary information for the objectives above, but should also offer us a more direct window on the physical processes operating in the jet as well as on the dynamics the jet itself. However, short time-coverage and under-sampling have prevented detailed temporal studies of blazars. Only a few such studies have been made in the past for blazars, e.g., evaluation of the energy dependent “time-lags” based on the synchrotron cooling picture. For example, by using *ASCA* data, Takahashi et al. (1996) argued the soft X-ray (< 1 keV) variation of Mrk 421, observed to lag behind that of the hard X-rays (≥ 2 keV) by ~ 4 ks, that may well be ascribed to the energy dependence of the synchrotron cooling timescale. More recently, Kataoka et al. (2000) interpreted an observed soft-lag and spectral evolution of PKS 2155-304 by a newly developed time-dependent synchrotron self-Compton (SSC) model.

The above *paradigm* of “soft-lag” was concerned, however, by several aspects. First, intensive X-ray monitoring of blazars has revealed not only soft lags but in some cases hard lags (Takahashi et al. 2000) which may be a manifestation of another process, e.g., energy dependent acceleration. Very recently, signature of hard lag was clearly observed in 1ES 1218+304, but this is so far an only example of manifestation of possible acceleration timescale in any TeV blazars (Sato et al. 2008; also in this volume). Second, as Edelson et al. (2001) voiced concerns, there was a question about the reliability of lags that are smaller than the orbital periods (~ 6 ks) of low Earth orbit satellites. This was refuted by Tanihata et al. (2001) and Zhang et al. (2004) who showed that, although periodic gaps introduce larger uncertainties than evenly sampled data, lags on hour-scale cannot be the result of periodic gaps. A time resolved cross correlation analysis of uninterrupted Mrk 421 data obtained by *XMM-Newton* revealed lags of both signs, changing on timescales of up to a few 10^3 s (Brinkmann et al. 2005). Hence the situation is very complex and still under debate.

Variability studies covering larger dynamic range and broader span of timescales have become common for Seyfert galaxies and Galactic black-holes (Edelson & Nandra 1999; Markowitz et al. 2004; McHardy et al. 2005; 2008 in this volume). From power spectrum density (PSD) analyses, it is well known that rapid fluctuations with frequency dependences $P(f) \propto f^{-1 \sim -2}$, are characteristic of time variability in accreting black hole systems (e.g., Hayashida et al. 1998). Although their physical origin is still under debate, some tentative scenarios have been suggested to account for these generic, fractal features (e.g., Kawaguchi et al. 2000). Similar studies have also been

proposed for blazars, but still underway. It has been suggested that X-ray variability of TeV blazars indicates a strong red-noise ($P(f) \propto f^{-2 \sim -3}$) behavior, compared to a fractal, flickering-noise of Seyfert galaxies (Kataoka et al. 2001).

These temporal studies are obviously important, however, special care must be taken if the data are not well sampled and relatively short compared to the variability timescale of the system. The prime motivation of this talk is to delineate the characteristic X-ray variability of TeV blazars, using a simple Monte Carlo simulation to evaluate the possible effects caused by observing time windows. Fortunately, we have now the *GLAST* mission successfully launched in June 2008, as well as various excellent missions/telescopes available through radio to TeV energy bands. Moreover, future X-ray missions including Monitor of All-sky X-ray Image (*MAXI*) is ready for launch early next year. A great advantage of *GLAST* and *MAXI* is to provide very uniform exposure all over the sky, that may shed new light on the temporal studies of blazars especially on longer timescale from a month to years.

2. Analysis Tools

2.1 Power Spectrum Density (PSD)

Power Spectrum Density (PSD) analysis is the most common technique used to characterize the variability of the system. An important issue is the data gaps, which are unavoidable for low-orbit X-ray satellites, such as *ASCA*, *RXTE*, and *BeppoSAX*. In these low-orbit satellites, Earth occultation makes periodic gaps every $\simeq 6$ ksec, even if we hope to make *continuous* monitoring observations. Similarly, previous long-look observations of various TeV blazars (e.g., Mrk 501 and PKS 2155–304 in Kataoka et al. 2001) inevitably faced serious artificial gaps, since the observations are spaced typically 3 or 4 orbits apart. To reduce the effects caused by such windowing, it is recommended to use a technique for calculating the PSD of unevenly sampled light curves.

Following Hayashida et al. (1998), the NPSD (*Normalized Power Spectrum Density*) at frequency f is defined as

$$\begin{aligned}
 P(f) &= \frac{[a^2(f) + b^2(f) - \sigma_{\text{stat}}^2/n]T}{F_{\text{av}}^2}, \\
 a(f) &= \frac{1}{n} \sum_{j=0}^{n-1} F_j \cos(2\pi f t_j), \\
 b(f) &= \frac{1}{n} \sum_{j=0}^{n-1} F_j \sin(2\pi f t_j),
 \end{aligned} \tag{2.1}$$

where F_j is the source count rate at time t_j ($0 \leq j \leq n-1$), T is the data length of the time series and F_{av} is the mean value of the source counting rate. The power due to the photon counting statistics is given by σ_{stat}^2 . With our definition, integration of power over the positive frequencies is equal to half of the light curve excess variance (e.g., Nandra et al. 1997).

To calculate the NPSD of certain data sets, it is recommended to make light curves of two different bin sizes shorter/longer than orbital gaps (e.g., 256 and 5760 sec, respectively). Each light curve is divided into “segments”, which are defined as the continuous part of the light curve.

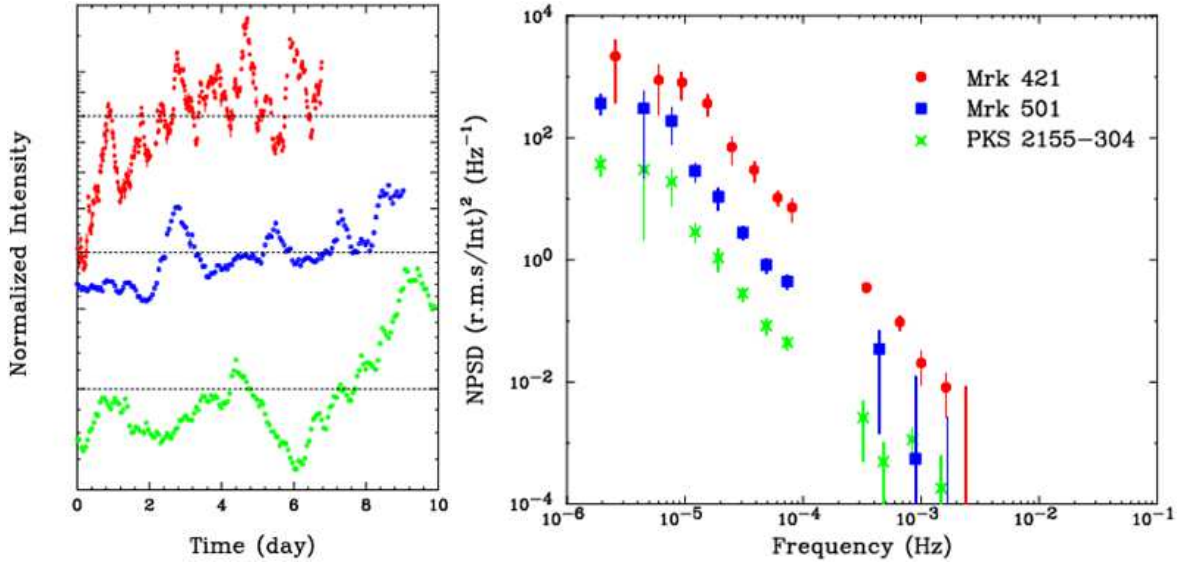


Figure 1: *left:* X-ray light curve of Mrk 421 (red), Mrk 501 (blue), and PKS 2155–304 (green) during intensive monitoring campaign with ASCA, measured in 0.7–7.5 keV band. Flux is normalized by their average intensities (dashed lines). *right:* Normalized PSD calculated from the light curves in the left panel. See Kataoka et al. 2001 and Tanihata 2001 for more details.

One can then calculate the power at frequencies $f = k/T$ ($1 \leq k \leq n/2$) for each segment and take the average. In this manner, the light curve binned at shorter timescale is divided into different segments every 5760 sec, corresponding to the gap due to orbital period. On the other hand, the light curve binned at 5760 sec is smoothly connected up to the total observation length T , if further artificial gaps are not involved. This technique produces a large blank in the NPSD at around 2×10^{-4} Hz (the inverse of the orbital period), but the effects caused by the sampling window are minimized.

Figure 1(*left*) shows examples of *observed* X-ray light curves of three TeV blazars, obtained during long (~ 10 day) monitoring with ASCA in 1998–2000 (red: Mrk 421, blue: Mrk 501; green: PKS 2155–304, respectively). Corresponding NPSDs are given in Figure 1(*right*). The upper frequency limit is the Nyquist frequency (2×10^{-3} Hz for 256 sec bins) and the lower frequency is about half the inverse of the longest continuous segments. These NPSDs are binned in logarithmic intervals of 0.2 (i.e. factors of 1.6) to reduce the noise. Note the NPSDs follow a power-law that decreases with increasing frequency in the high-frequency range (typically, $P(f) \propto f^{-2.5}$). Possible signs of a roll-over can be seen at the low-frequency end ($f_{\text{br}} \sim 10^{-5}$ Hz). Below this break, the NPSD becomes significantly flatter, such that $P(f) \propto f^{-1.0}$. Since all the NPSDs have very steep power-law slopes, only little power exists above 10^{-3} Hz. This is very different from the PSDs of Seyfert galaxies, for which powers are well above the counting noise up to 10^{-2} Hz (e.g., Hayashida et al. 1998; Nowak & Chiang 2000).

Finally, we revisit the effects caused by sampling windows. As mentioned above, our PSD technique is less affected by the sampling windows, because only the continuous parts of the light curve are used for the calculation. In fact, this seems to have negligible effects for the present data, because the interruptions are almost even and the observing efficiency is high (~ 0.5). The most

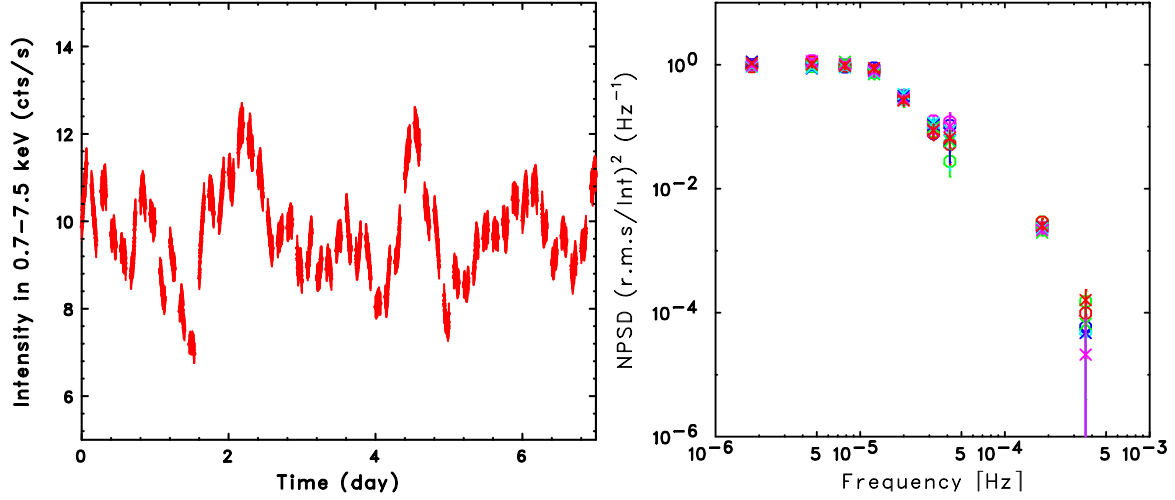


Figure 2: *left:* An example of simulated light curve described in the text. *right:* Examples of normalized PSD calculated from 10 simulated light curves.

rigorous estimate of this effect would be obtained by simulating the light curves characterized with a certain PSD, filtered by the same window as the actual observation. The resulting PSDs could then be compared with that we assumed. For this purpose, using a Monte Carlo technique, we generate a set of random numbers uniformly distributed between 0 and 2π and use them as the random phases of the Fourier components. A fake light curve is then generated by a Fourier transformation, with the constraint that the power in each frequency bin decreases as specified by the PSD. We simply choose a deterministic amplitude for each frequency and randomize only the phases, a common approach (e.g., Done et al. 1989). It may be most rigorous to also assume “random amplitudes” distributed within 1σ of the input PSD (Timmer & König 1995), but simulations based on their algorithm remain as a future work.

Figure 2 (*left*) shows an example light curve thus produced, with a hypothesized PSD of the form; $P(f) = P_0 f^{-2.5}$ ($f \geq f_{\text{br}}$) and $P(f) = P_0$ ($f \leq f_{\text{br}}$), where $f_{\text{br}} = 10^{-5}$ Hz. We have made hundreds of such pseudo light curves and calculated the PSD as actual observational data. Right panel shows the PSDs plotted for 10 sets of such light curves. One can see that even when the orbital gaps are present, the resultant PSD is not affected seriously, and hence we can safely determine the original PSD which produces the observed light curves.

2.2 Structure Function (SF)

Next we examine the use of a numerical technique called the structure function (hereafter, SF). The SF can potentially provide information on the nature of the physical process causing any observed variability. While in theory the SF is completely equivalent to traditional Fourier analysis methods (e.g., the NPSD; § 2.1), it has several significant advantages. Firstly, it is much easier to calculate. Secondly, the SF is less affected by gaps in the light curves (e.g., Hughes et al. 1992). The definitions of SFs and their properties are given by Simonetti et al. (1985). The first order SF is defined as

$$\text{SF}(\tau) = \frac{1}{N} \sum [a(t) - a(t + \tau)]^2, \quad (2.2)$$

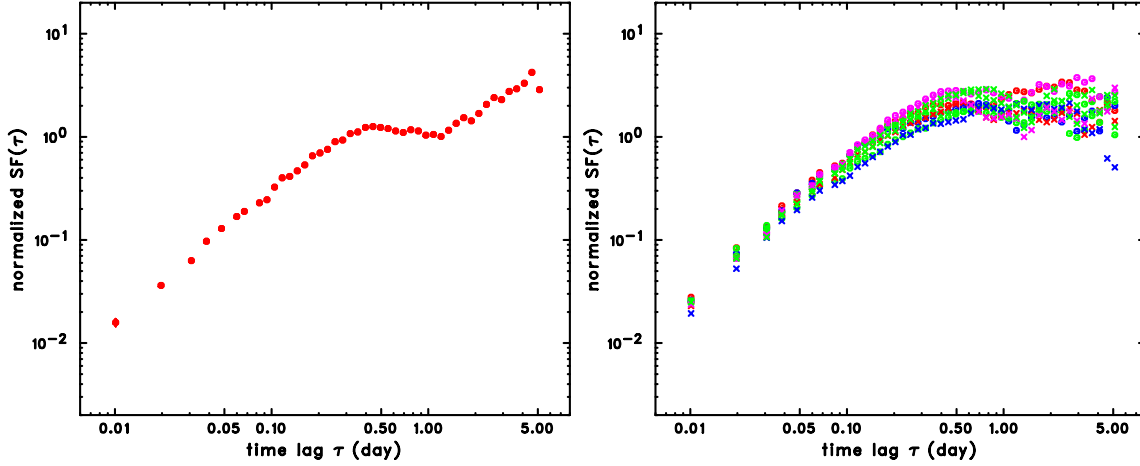


Figure 3: *left:* Structure function calculated from the observed light curve of Mrk 421 with ASCA (see Figure 1 *left*). *right:* Structure function calculated from the simulated light curves to see the effects caused by finite length of data.

where $a(t)$ is a point of the time series (light curves) $\{a\}$ and the summation is made over all pairs separated in time by τ . N is the number of such pairs. More rigorously, minor modification is suggested in Tanihata et al. (2001), that one should use a continuous weighting factor proportional to its significance of each data point when the flux uncertainties are non-uniform. Note that the SF is free from the DC component in the time series, whereas techniques such as the auto-correlation function (ACF) and the PSD are not.

The SF is closely related with the power spectrum density (PSD) distribution. If the structure function has a power-law form, $SF(\tau) \propto \tau^\beta$ ($\beta > 0$), then the power spectrum has the distribution $P(f) \propto f^{-\alpha}$, where f is frequency and $\alpha \simeq \beta + 1$. We note that this approximation is invalid when α is smaller than 1. In fact, both the SF and the NPSD should have zero slope for white noise, because it has zero correlation timescale. However, the relation holds within an error of $\Delta\alpha \simeq 0.2$ when α is larger than ~ 1.5 (e.g., Paltani et al. 1997; Cagnoni, Papadakis & Fruscone 2001; Iyomoto & Makishima 2000). Therefore the SF gives a crude but convenient estimate of the corresponding PSD distribution which characterizes the variability.

In general, the SF gradually changes its slope (β) with time interval τ . On the shortest timescale, variability can be well approximated by a linear function of time; $a(t) \propto t$. In this time domain, the resulting SF is $\propto \tau^2$, which is the steepest portion in the SF curve. For longer timescales, the slope of the SF becomes flatter ($\beta < 2$) reflecting the physical process operating in the system. When τ exceeds the longest time variability of the system, the SF further flattens, with $\beta \sim 0$, which is the flattest portion in the SF curve (white noise). At this end, the amplitude of the SF is equal to twice the variance of the fluctuation. In Figure 3 (*left*), the SF is calculated for the light curves of Mrk 421 presented in Figure 1 (*left*). The resulting SF is normalized by the square of the mean fluxes, and are binned at logarithmically equal intervals. Note that the SF is characterized with a steep increase ($\beta > 1$) in the time region of $10^{-2} < \tau/\text{day} < 1$, roughly consistent with the corresponding NPSDs given in Figure 2 ($P(f) \propto f^{-2.5}$).

The SFs of the X-ray light curves show a variety of features. For example, the SF of Mrk 421

(Figure 3 (*left*)) shows a complex SF that cannot even be described as a simple power-law, as it flattens around 0.5 day, then steepens again around 2 days. A similar “roll-over” can be seen for the SF of Mrk 501 and PKS 2155–304 around 1 day (Tanihata et al. 2001). Importantly, these turn-overs reflect the typical timescale of repeated flares, corresponding to the break in the NPSDs described in § 2.1. The complicated features (rapid rise and decay) at large τ may not be real and may result from the insufficiently long sampling of data. The number of pairs in Equation (2.2) decreases with increasing τ , and hence the resulting SF becomes uncertain as τ approaches T , where T is the total length of time series. The statistical significance of these features can be easily tested using the Monte Carlo simulation. Figure 3 (*right*) shows a set of SFs calculated by assuming the same PSD described in the previous section ($P(f) = P_0 f^{-2.5}$ for $f \geq f_{\text{br}}$, where $f_{\text{br}} = 10^{-5}$ Hz). Note we have simulated the light curves more than 5 times longer than actual observation. One can see although the resultant SFs well agree below the break, wide variety exists if $\tau \gtrsim 1/3 T$ due to uncertainties caused by finite length of data. Therefore special care must be taken for possible artifacts near $\tau_{\text{max}} = T$.

We next calculate the structure functions using all available X-ray data set between 1993 and 1998 for Mrk 421. Using 5 year’s ASCA data, we can investigate the variability in the widest time domain over more than five orders; $10^{-2} \leq \tau/\text{day} \leq 10^3$. Figure 4 (*left*) shows a light curve thus produced, while the SF is given in Figure 4 (*right*). *Filled circles* are observational data, normalized by the square of the mean fluxes, and are binned at logarithmically equal intervals. The SF shows a rapid increase up to $\tau/\text{day} \simeq 1$, then gradually flatten to the observed longest timescale of $\tau/\text{day} \geq 1000$. Fluctuations at large τ ($\tau/\text{day} \geq 10$) are due to the extremely sparse sampling of data. Although we cannot apply the usual PSD technique to such under-sampled data, it appears the SF still can be a viable estimator.

In order to demonstrate the uncertainties caused by such sparse sampling, and to firmly establish the reality of the “roll-over”, we simulate the long-term light curves following the Monte Carlo method described above. We first applied this technique assuming a PSD of the form $P(f) \propto f^{-\alpha}$, where α is determined from the best fit NPSD parameters given in Figure 1. Based on a set of a thousand fake light curves, we computed the expected mean value, $\langle SF_{\text{sim}}(\tau) \rangle$, and variance, $\sigma_{SF(\tau)}$, of all the simulated SFs at each τ . The results are superimposed in Figure 5(b) as *crosses*. Errors on simulated data points are equal to $\pm \sigma_{SF(\tau)}$. One finds that errors become larger at large τ , meaning that the SF tends to involve fake bumps and wiggles near the longest observed timescale. Large deviations between the actual SFs (*filled circles*) and the simulated ones (*crosses*) are apparent, but quantitative comparison with actual data is necessary.

To evaluate the statistical significance of the goodness of fit, and to test the reality of complicated features in the SF, we then calculate the sum of squared differences,

$\chi_{\text{sim}}^2 = \sum_k \{ \log[\langle SF_{\text{sim}}(\tau_k) \rangle] - \log[SF(\tau_k)] \}^2$. Strictly speaking, “ χ_{sim}^2 ” defined here is different from the traditional χ^2 , but the statistical meaning is the same. For the actual SFs, these values are $\chi_{\text{sim}}^2 = 1608$ for Mrk 421. We then generated *another* set of 1,000 simulated light curves and hence fake SFs to evaluate the the distribution of χ_{sim}^2 values. From this simulation, the probability that the X-ray light curves are the realization of the assumed PSDs (i.e., a simple power-law) is $P(\chi^2) < 10^{-3}$. We thus introduce a “break”, below which the slope of the PSD becomes flatter. Since the exact position of a break is not well constrained, we simulate various cases of $f_{\text{br}} = 3.9 \times 10^{-5}$, 1.2×10^{-5} , and 3.9×10^{-6} Hz, which correspond to the break in the SF at $\tau/\text{day} \simeq 0.3, 1, 3$, respec-

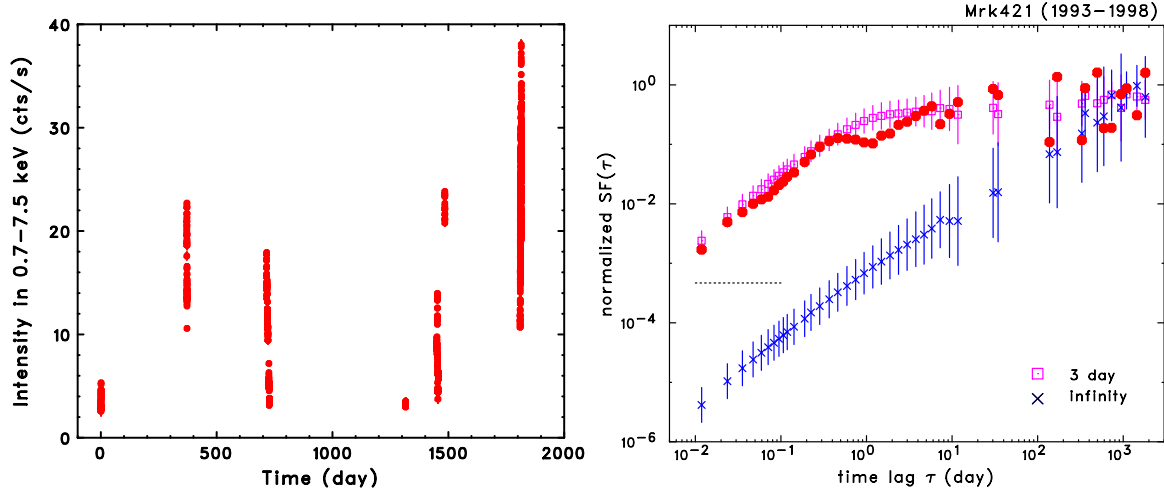


Figure 4: *left:* Long-term X-ray flux variation of Mrk 421 between 1993 and 1998, measured in 0.7–7.5 keV band. *right:* Structure function of Mrk 421 based on long-term light curves presented in the *left* panel. *Filled circles* represent the observational data, *crosses* represent simulated SF assuming a single-power-law NPSD, and *open squares* represent simulated SF assuming a broken power-law NPSD. Full details are given in the text.

tively. As a result, the statistical significance is significantly improved. Result is given in Figure 4 (*right*) as *open squares*. For Mrk 421, best fit χ^2 was obtained when $f_{\text{br}} = 3.9 \times 10^{-6}$ Hz ($\chi^2 = 47$; $P(\chi^2) = 0.59$). We thus conclude that (1) the PSD of the TeV sources have at least one roll-over at $10^{-6} \text{ Hz} \leq f_{\text{br}} \leq 10^{-5} \text{ Hz}$ ($1 \leq \tau/\text{day} \leq 10$), and (2) the PSD changes its slope from $\propto f^{-1 \sim -2}$ ($f < f_{\text{br}}$) to $\propto f^{-2 \sim -3}$ ($f > f_{\text{br}}$) around the roll-over.

2.3 Discrete Correlation Function (DCF)

In order to compare the time series in various energy bands quantitatively, we introduce the discrete correlation function given by Edelson & Krolik (1988). This technique was specifically designed to analyze unevenly sampled data sets. The first step is to calculate the set of unbinned discrete correlations (UDCF) between each data point in the two data streams. This is defined in the time domain as

$$\text{UDCF}_{ij} = \frac{(a_i - \bar{a})(b_j - \bar{b})}{\sqrt{\sigma_a^2 \sigma_b^2}}, \quad (2.3)$$

where a_i and b_j are points of the data set $\{a\}$ and $\{b\}$, \bar{a} and \bar{b} are the means of the data sets, and σ_a and σ_b are the standard deviation of each data set. The discrete correlation function (DCF) for each time lag τ is defined as an average of the UDCF that have the same τ ,

$$\text{DCF}(\tau) = \frac{1}{M} \sum \text{UDCF}_{ij}(\tau), \quad (2.4)$$

where M is the number of pairs in the bin.

The DCF advantages are that it uses all the data points available, does not introduce new errors through interpolation, and calculates a meaningful error estimates. The standard error for each bin

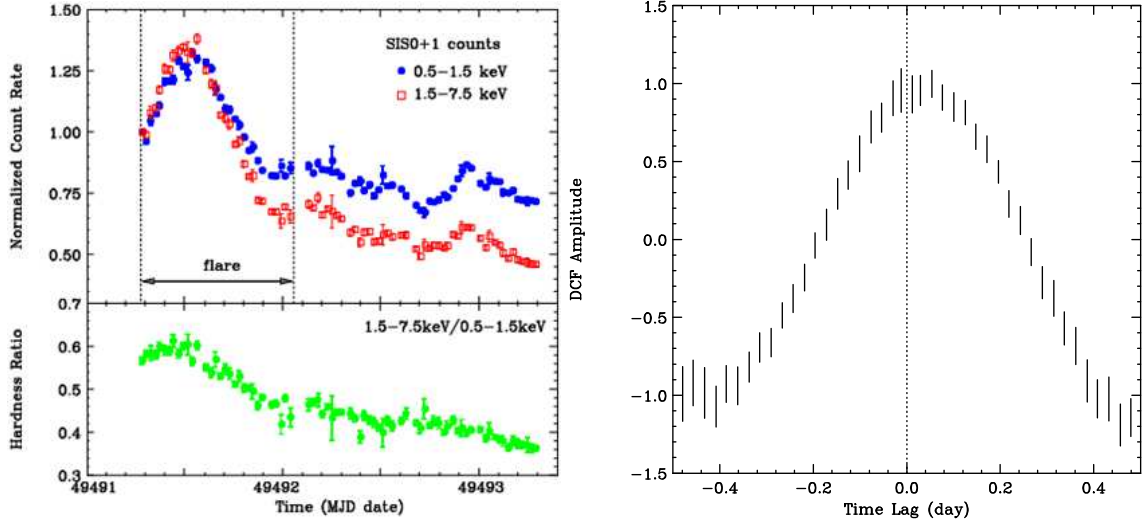


Figure 5: *left:* Time history of the X-ray emission of PKS 2155–304 during 1994 observation with ASCA. Upper panel represents the X-ray right curves measured in 0.5–1.5 keV and 1.5–7.5 keV, respectively, while the bottom panel shows the time history of hardness ratio. *right:* Discrete correlation function of PKS 2155–304 calculated from the light curves in the *left* panel. Time lags in 0.5–1.0 keV band was calculated as compared to that in the 3.0–7.5 keV band.

is calculated as

$$\sigma_{\text{DCF}} = \frac{1}{M-1} (\sum [\text{UDCF}_{ij} - \text{DCF}(\tau)]^2)^{1/2}. \quad (2.5)$$

As an application, Figure 5 shows an example to see time-lag in the light curve of PKS 2155–304 (Kataoka et al. 2000). The data reveal a large flare at the beginning, followed by lower amplitude fluctuations. The source variability is somewhat different in different energy bands. Notably, amplitude of flux change is larger at higher photon energies; a factor of 2 at 1.5–7.5 keV (red), while it is a factor of 1.5 in the 0.5–1.5 keV (blue). Also note that the peak of the light curve in the hard X-ray bands leads that in the soft X-ray bands by ~ 4 –5 ksec. This was also suggested by direct fitting of the light curves with a simple Gaussian plus constant offset, resulting that a lag of the peaking time by $\simeq 4$ ksec. We therefore computed the cross correlations using the DCF by dividing the 0.5–7.5 keV range into five energy bands and measured the time lag for each light curve compared to the 3.0–7.5 keV light curve. The results are shown in Figure 5 (*right*), again suggesting $\simeq 4$ ksec lags in the X-ray variability of PKS 2155–304.

As we have seen in §1, reality of this small amount of lag is still matter of debate, due to the periodic gaps (~ 6 ks) of low-Earth orbit satellites (e.g., Edelson et al. 2001). Meanwhile, it is also suggested that lags on hour-scale can hardly be produced by periodic gaps based on careful simulations (e.g., Tanihata et al. 2001; Zhang et al. 2004). To quickly follow their arguments, I have made hundreds pairs of light curves by Monte Carlo simulation, one of which is artificially “lagged” by 4 ksec. Then the resultant light curves are filtered by the same window as the actual observation. Figure 6 (*left*) shows an example pair of light curves thus produced, and Figure 6 (*right*) shows the calculated DCF for 10 pairs of light curves. It seems that the DCF exhibits large uncertainties but the peak of the DCF is always retained as expected (i.e., 4 ksec). Obviously, higher quality X-ray data which are less affected by window sampling is strongly awaited for

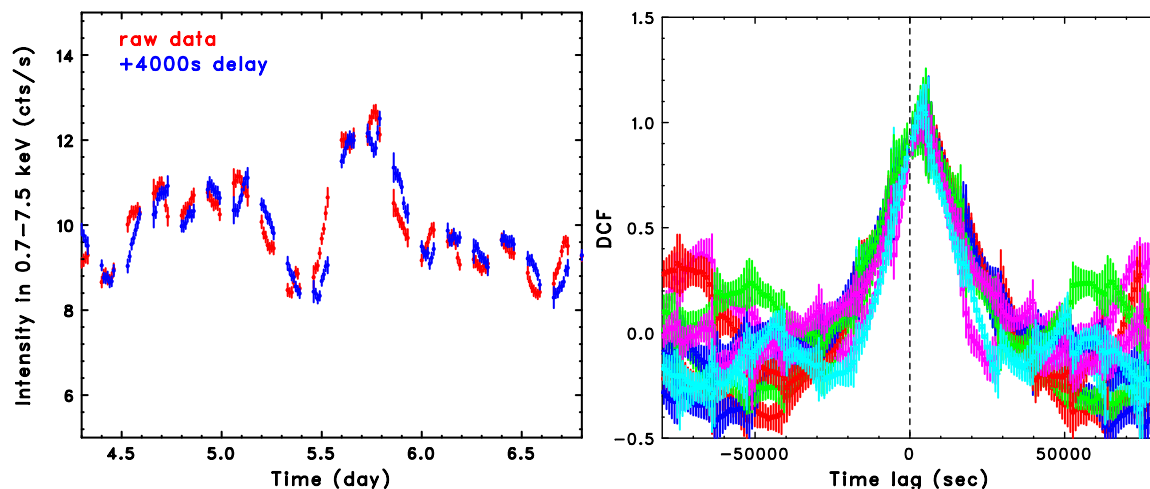


Figure 6: *left:* An example of simulated light curve to evaluate the effects caused by orbital gap in the measurement of time lag. *right:* Examples of DCFs calculated from artificially lagged (by 4000 sec) light curves.

further clarification of this long standing problem. At this point, it is also worth noting the most recent observation of a TeV blazar 1ES 1218+304 exhibiting a clear signature of time-lag which is much larger than the orbital gap (~ 20 ksec), but in the opposite sense (so-called “hard-lag”). For more detail, see Sato et al. 2008 in this volume.

3. Future Prospects; *GLAST* and *MAXI*

In the previous sections, we showed that temporal techniques, such as PSD, SF and DCF are indeed powerful tools to understand the nature of variability in blazars, as long as various artifacts are correctly taken into account. We showed that the Monte Carlo simulation is the one of the best way to evaluate possible artifacts caused by window sampling as well as finite length of data. These approaches, however, are very time-consuming works and somewhat conservative for future progress. Very fortunately, we will have two important missions to uniformly/densely observe celestial sources in the high energy regime: *GLAST* and *MAXI*. In particular, *GLAST* was successfully launched June 11, 2008, and the activation of the LAT (Large Area Telescope) is about to begin (Madejski et al. 2008 in this volume).

It is widely expected that *GLAST* will detect a large number (probably between 3,000 and 10,000) of extragalactic sources, most of which will be identified as blazars. Moreover, the LAT large field-of-view combined with scanning mode will provide a very uniform exposure over the sky, allowing constant monitoring of all detected blazars and flare alerts to be issued. Apparently, simultaneous multiwavelength campaigns are essentially important for both “EGRET blazars” (i.e., well-established sources) as well as newly detected γ -ray sources. In X-ray, many observatories are already being actively prepared. For example, we are planning dedicated campaigns of 7 quasar hosted blazars (QHBs) as a part of *Suzaku*-AO3 as listed in Table 1. Assuming a large flare as that observed for 3C 279 in 1991, *Suzaku* can determine the X-ray spectrum up to 300 keV with

Source Name	Redshift	Class	Flux (2-10 keV) [10^{-12} erg/cm ² /s]	Flux (≥ 100 MeV) [10^{-5} ph/cm ² /s]
PKS 0208-512	1.00	HPQ	9.5	85.5 \pm 4.5
Q 0827+243	0.94	LPQ	4.8	24.9 \pm 3.9
PKS 1127-145	1.18	LPQ	11.0	38.3 \pm 8.0
PKS 1510-089	0.36	LPQ	10.0	18.0 \pm 3.8
3C 454.3	0.86	HPQ	11.0	53.7 \pm 4.0
3C 279	0.54	HPQ	13.0	89.0 \pm 3.2
PKS 0528+134	2.06	LPQ	30.0	60.0 \pm 3.0

Table 1: A list of “VIP” blazars to be simultaneously observed with *GLAST* and *Suzaku* in 2008/09.

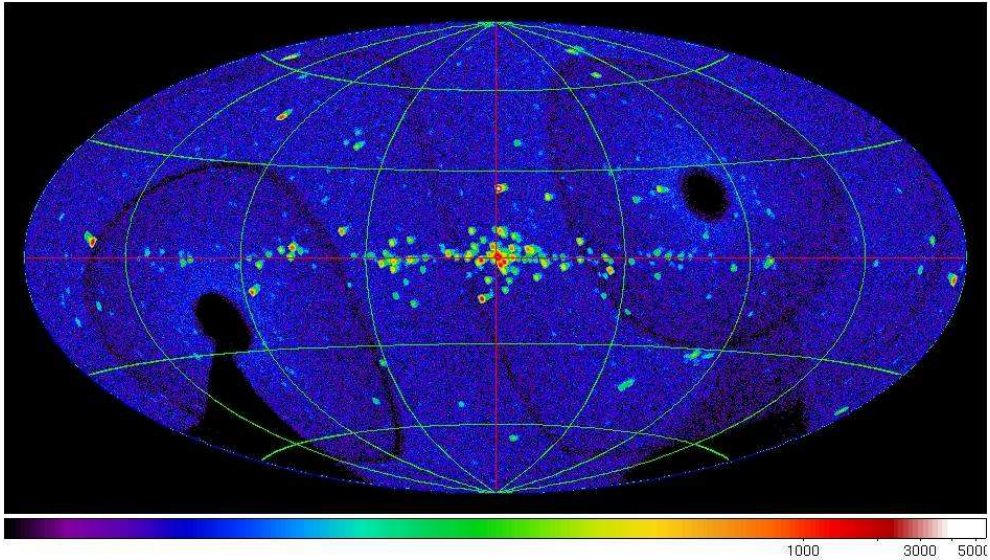


Figure 7: An expected X-ray sky map for 1 day exposure with *MAXI*.

an unprecedented accuracy. Coordinated observations between *GLAST* and X-ray satellites are crucial for further understanding the nature of various types of blazars.

Another important mission for future blazar studies will be the Monitor of All-sky X-ray Image (*MAXI*). *MAXI* is an X-ray all-sky monitor which is currently scheduled to be attached to the Japanese Experiment Module - Exposed Facility (JEM-EF) on the International Space Station (ISS) in early 2009. The *MAXI* carries two scientific instruments: the Gas Slit Camera (GSC) and the Solid State-slit Camera (SSC). The GSC consists of position-sensitive proportional counters with large collecting area of 5350 cm² in 2–30 keV range, while the SSC is utilizing 32 X-ray CCD chips covering an energy range of 0.5–12 keV. The *MAXI* has two sets of GSC and SSC orthogonally oriented, each of which covers a narrow instantaneous field of view of 1.5 deg times 160 deg that sweeps over the whole sky during every orbit of 90 minutes. Thus a certain sky area is generally monitored twice in an orbit. The expected detection sensitivity for the GSC is ~ 5 mCrab in a day and ~ 1 mCrab in one month, which is higher by a factor of 5 than that of

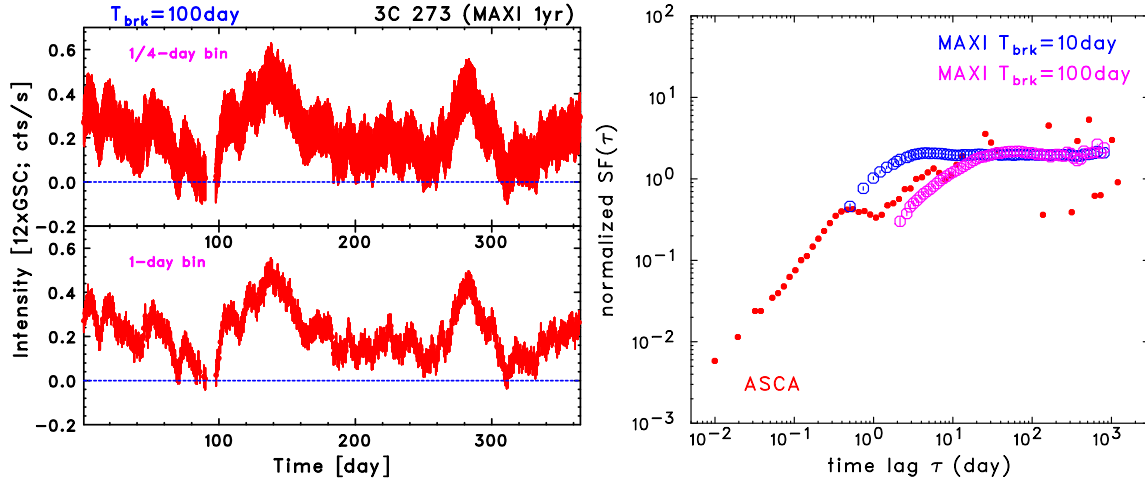


Figure 8: *left:* Simulation of 3C 273 light curve observed with *MAXI*. Data are binned at 0.25 day (*upper*) and 1 day (*lower*), respectively. *right:* Structure function of Mrk 421 calculated from the simulated light curves with *MAXI* as a 10 mCrab source.

RXTE/ASM. Such a high sensitivity and its monitor capability are very useful in study of AGNs, compact sources such as microquasars and Galactic blackholes.

Figure 7 shows the expected X-ray sky map for 1 day exposure with *MAXI*. Bright AGNs, such as 3C 273 ($\simeq 5$ mCrab) and Mrk 421 ($\simeq 10$ mCrab) can be detected with more than 5σ level everyday, allowing for the first time non-bias monitoring of the sources from a day to more than year scale. Figure 8 (*left*) shows the simulated long-term (1 year) light curve of 3C 273, assuming a PSD slope of 2.0 with break time scale of $1/f_{\text{brk}} \simeq 100$ day. The resultant structure function of the light curve, presented as Figure 8 (*right*), clearly reveals variability nature of blazars on extremely longer timescale than the characteristic break. It is suggested that these long-term trend may be produced by the time variation of accreting matter near the central black hole, as well as the duty cycle of mass ejection to the relativistic jet, which provide important challenges to blazars in the next decade.

References

- [1] Aharonian, F., et al. 2007, *ApJ*, 664, L71
- [2] Albert, J., et al. 2007, *ApJ*, 669, 862
- [3] Brinkmann, W., Papadakis, I. E., Raeth, C., Mimica, P., & Haberl, F. 2005, *A&A*, 443, 397
- [4] Cagnoni, I., Papadakis, I. E., & Fruscione, A., 2001, *ApJ*, 546, 886
- [5] Done, C., Madejski, G. M., & Mushotzky, R. F., et al., 1989, *ApJ*, 400, 138
- [6] Edelson, R., & Krolik, J. H. 1988, *ApJ*, 333, 646
- [7] Edelson, R., & Nandra, K., 1999, *ApJ*, 514, 682
- [8] Edelson, R. et al. 2001, *ApJ*, 554, 274
- [9] Hayashida, K., et al. 1998, *ApJ*, 500, 642

- [10] Hughes, P. A., Aller, H. D., & Aller, M. F., 1992, *ApJ*, 396, 469
- [11] Inoue, S. & Takahara, F. 1996, *ApJ*, 463, 555
- [12] Iyomoto, N., & Makishima, K., 2001, *MNRAS*, 321, 767
- [13] Kataoka, J., et al. 2000, *ApJ*, 528, 243
- [14] Kataoka, J., et al. 2001, *ApJ*, 560, 659
- [15] Kawaguchi, T., et al. 2000, *PASJ*, 52, L1
- [16] Kirk, J., Ringer, F., & Mastichiadis, A. 1998, *A&A*, 333, 452
- [17] Madejski, G. M., et al. 2008, in this volume
- [18] Markowitz, A., & Edelson, R., 2004, *ApJ*, 617, 939
- [19] McHardy, I. M., Gunn, K. F., Uttley, P., & Goad, M. R. 2005, *MNRAS*, 359, 345
- [20] McHardy, I. M., et al. 2008, in this volume
- [21] Nandra, K., et al. 1997, *ApJ*, 476, 70
- [22] Nowak, M, A., & Chiang, J, 2000, *ApJ*, 531, L13
- [23] Paltani, S., et al. 1997, 327, 539
- [24] Sato, R., Kataoka, J., Takahashi, T., Madejski, G. M., Rugamer, S., and Wagner, S. J., *ApJ*, 680, L9
- [25] Sato, R., et al. in this volume
- [26] Simonetti, J. H., Cordes, J. M., & Heeschen, D. S., 1985, *ApJ*, 296, 46
- [27] Takahashi, T. et al. 1996, *ApJ*, 470, L89
- [28] Takahashi, T. et al. 2000, *ApJ*, 542, L105
- [29] Tanihata, C., Urry, C. M., Takahashi, T., Kataoka, J. et al. 2001, *ApJ*, 563, 569
- [30] Timmer, J., & König, M., 1995, *A & A*, 300, 700
- [31] Zhang, Y. H., Cagnori, I., Treves, A., Celotti, A., & Maraschi, L. 2004, *ApJ*, 605, 98